THE JOURNAL OF PHYSICAL CHEMISTRY C
A JOURNAL OF THE AMERICAN CHEMICAL SOCIETY
pubs.acs.org/JPCC
Article

Dependence of Electron–Hole Recombination Rates on Charge Carrier Concentration: A Case Study of Nonadiabatic Molecular Dynamics in Graphitic Carbon Nitride Monolayers

Published as part of The Journal of Physical Chemistry virtual special issue "Early-Career and Emerging Researchers in Physical Chemistry Volume 2".

Mohammad Shakiba and Alexey V. Akimov*

Cite This: *J. Phys. Chem. C* 2023, 127, 9083–9096 **Read Online**

ACCESS | Metrics & More | Article Recommendations | Supporting Information

ABSTRACT: Through systematic nonadiabatic molecular dynamics (NA-MD) calculations in a prototypical graphitic carbon nitride (C_3N_4) monolayer, we demonstrate a strong dependence of electron–hole recombination time scales on the size of the simulation supercell and hence on the formal concentration of charge carriers. Using our recently developed NA-MD methodology with extended tight-binding electronic structure calculations, we have been able to conduct such calculations in C_3N_4 monolayers containing up to 5600 atoms. The predicted time scales vary from 7 ps in the smallest (2 × 2) systems to 23 ns in the largest (8 × 8, 10 × 10) ones and depend on the NA-MD methodology and the basis of electronic excitations used. The concentration dependence becomes negligible only in very large systems, such as 8 × 8 or 10 × 10 supercells. In this limit, the time scales also become insensitive to the number of electronic excitations used in NA-MD calculations and to the inclusion of decoherence effects. We propose an effective state reduction model to explain this result.

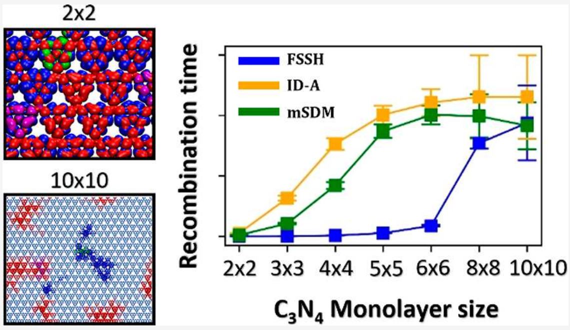

1. INTRODUCTION

Nonadiabatic (NA) molecular dynamics (MD) provides valuable insights into excited state dynamics in many classes of solar energy materials such as light-harvesting systems,[1−18] light-emitting diodes,[19] and photocatalytic materials.[20−22] The efficiency of photoinduced processes such as charge carrier injection, relaxation, and electron–hole (e–h) recombination in these materials can be described using NA-MD simulations. Although such calculations have provided multiple insights into the functioning of solar energy materials,[1−3,6,8,12−14,17,18] helped rationalize numerous experiments,[13,15,16,21,23−26] and revealed valuable trends,[11,27−32] the direct connection of the obtained computational results with the experimental observations and measurements remains a challenge. One of the puzzles to be solved before this connection can be established is the realization that the concentration of the photoinduced charge carrier present in typical simulations is notably overestimated compared to that observed experimentally in realistic materials.[33−35] Due to the computational complexity of typical NA-MD calculations, it is customary to employ only small or medium-sized simulation cells in NA-MD studies[2,7,11,27,36−38] and assume that the effects of charge carrier concentration are negligible. However, the influence of charge carrier (electrons, holes, and excitons) concentration and simulation cell size on the recombination and excited state relaxation dynamics remains a rather obscure area. In a recent review that we became aware of during the revision of this paper, Wang and co-workers[39] brought the topic of the dependence of carrier lifetimes on the carrier concentration to the attention of the community. With simple estimates, the authors "converted" the time scales directly computed from NA-MD calculations to what could be experimentally measured carrier lifetimes. The two quantities are typically separated apart by several orders of magnitude, solely due to carrier concentration effects.

One way to explore the role of charge carrier concentration in their dynamics is by modeling it in unit cells of a systematically increased size, ideally such that they could approach the experimentally relevant charge carrier concentrations. In experiments, the intrinsic charge carrier concentration in two-dimensional materials varies in the range ~10^{10}–10^{13} cm^{-2}.[12,40,41] In order to capture this charge

Received: January 10, 2023
Revised: March 13, 2023
Published: May 3, 2023

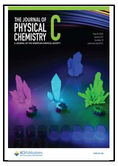

https://doi.org/10.1021/acs.jpcc.3c00211
J. Phys. Chem. C 2023, 127, 9083–9096

carrier density in theory, one needs to consider monolayers as large as ∼3−100 nm in width. However, modeling excited state dynamics for a huge supercell size of 100 nm × 100 nm that involves hundreds of thousands of atoms is computationally not feasible. Nonetheless, one may still explore the concentration effect in much smaller supercells, although exceeding those that are typically used by NA-MD practitioners.

Recently, we have developed an NA-MD methodology[27] that relies on the extended tight-binding (xTB) electronic structure method[42−44] applicable to very large atomistic systems, with thousands of atoms. The xTB method has been proposed by Bannwarth et al.[42−44] as a new tight-binding approach that provides parametrization for a wide range of elements, up to $Z = 86$, and can be applied to large-scale structures with thousands of atoms. The extensive parametrization of the method makes it more attractive to materials' problems than the more conventional density functional tight-binding (DFTB)[45−51] or semiempirical methods.[52−55] The latter may be more suitable for biological and organic molecules. The xTB method has also been successful in describing quantum mechanical properties such as absorption spectra in different organic and inorganic materials including proteins[44,56,57] and metal−organic frameworks (MOFs)[58] at a reasonable computational cost.

In this study, we utilize our xTB/NA-MD to address the above question on the role of charge carrier concentration in NA dynamics. We focus on e−h recombination dynamics in graphitic carbon nitride (C_3N_4) monolayers of varied sizes. This material has recently attracted a lot of interest as a promising nontoxic material for photocatalytic water splitting[35,59−61] and CO_2 photoreduction.[33,34] In the past few years, the NA-MD studies of e−h recombination dynamics in pristine, defect-containing, and doped graphitic C_3N_4 monolayers have been reported by Agrawal et al.,[37,62,63] who utilized simulation cells with only up to 50 atoms and found that dual defects and boron doping in graphitic C_3N_4 monolayers helped enhance the e−h recombination lifetime. Similar NA-MD studies have been conducted for other types of 2D materials, such as black phosphorus[36,64−66] or transition metal dichalcogenide[7,15,67] monolayers where small super cells with up to 100 atoms were adopted. Earlier, we were able to model NA-MD in bigger C_3N_4 supercells, containing up to 224 atoms.[27] Nonetheless, even such sizes lead to overestimated charge carrier concentrations. In the present work, we further extend the size of the simulation cell, up to 14.5 nm × 12 nm and containing as many as 5600 atoms. While even this advancement of the simulation protocol does not give us access to the charge carrier concentrations relevant to experiments, it enables us to investigate the dependence of the carrier dynamics on the carrier concentrations with the latter varying over several orders of magnitude.

In the present work, we investigate the role of charge carrier concentration on e−h recombination time scales by conducting a series of direct NA-MD simulations in C_3N_4 supercells of systematically increased size. We first discuss differences in nuclear dynamics and electronic structure in such systems, paying special attention to the topic of molecular orbital (MO) localization. We then discuss trends in the NA coupling (NAC) magnitudes, their distribution functions, and their dependencies on the monolayer size. We analyze the results of explicit NA-MD calculations of e−h recombination dynamics using several trajectory surface hopping (TSH) methods. We pay attention to the convergence of the computed time scales with the system size and to the rate of this convergence as a function of computational methodology used. In particular, we discuss the role of electronic decoherence and the basis of excited states used in the calculations. Interestingly, the role of these factors becomes negligible in the largest systems considered. We attribute this observation to a reduction of a many-state dynamics to an effective two-state dynamics.

2. THEORY AND METHODS

2.1. NA-MD Theory.

The NA-MD approach used in this work is briefly summarized below. For more details, we refer the reader to relevant reviews[55,68−70] and implementation works.[27,28] The evolution of the system's electron−nuclear wave function, $\Psi(r, R, t)$, is given by the time-dependent Schrödinger equation (TD-SE):

$$i\hbar \frac{\partial \Psi(r, R, t)}{\partial t} = \hat{H}(r, R, t)\, \Psi(r, R, t) \tag{1a}$$

in which $\hat{H}(r, R, t)$ is the system's Hamiltonian. Within the quantum-classical path approximation,[71,72] the nuclei are treated classically, and their evolution is described by solving Newtonian equations of motion on the corresponding adiabatic energy surfaces; the electrons are treated quantum mechanically and are described by the electronic wave function that is parametrized by classical trajectories, $R(t)$ $\Psi(r, t; R(t))$. Along with the replacement of the full electron−nuclear wave function, $\Psi(r, R, t)$, by the quantum-classical one, $\Psi(r, t; R(t))$ the Hamiltonian $\hat{H}(r, R, t)$ is also replaced by a corresponding quantum-classical counterpart, $\hat{H}(r, R, t) \rightarrow \hat{H}(r, t; R(t))$, so the TD-SE being solved is

$$i\hbar \frac{\partial \Psi(r, t; R(t))}{\partial t} = \hat{H}(r, t; R(t))\, \Psi(r, t; R(t)) \tag{1b}$$

The electronic wave function $\Psi(r, t; R(t))$ is expanded in the basis of the electronic Hamiltonian eigenfunctions, $\psi_i(r, t; R(t))$, that are known as adiabatic electronic wave functions:

$$\Psi(r, t; R(t)) = \sum_i c_i(t)\, \psi_i(r, t; R(t)) \tag{2}$$

Here, $c_i(t)$ are the time-dependent amplitudes that correspond to the adiabatic basis functions. Considering eq 2, the TD-SE eq 3 can be brought to the form

$$i\hbar \dot{c}_i = \sum_j H_{ij}^{\mathrm{vib}}(t)\, c_j(t) \tag{3}$$

$$H_{ij}^{\mathrm{vib}} = E_j \delta_{ij} - i\hbar d_{ij} \tag{4}$$

Here, E_j is the energy of the jth state and d_{ij} is the NAC value between states j and i and equals

$$d_{ij} = \left\langle \psi_i \middle| \frac{\partial}{\partial t} \middle| \psi_j \right\rangle \tag{5}$$

The coherently evolved amplitudes, $c_i(t)$, are used to compute the probabilities of electronic state change for each trajectory. We use the fewest switches surface hopping (FSSH) algorithm of Tully.[72] Within the FSSH, a state i is proposed to switch to a state j at every time step with the probability of

$$P_{i\to j}(t, t+\Delta t) = \max\left(0, \frac{\Delta t}{\rho_{ii}}\,\mathrm{Im}(\rho_{ij}H^{\mathrm{vib}}_{ji} - H^{\mathrm{vib}}_{ij}\rho_{ji})\right),\quad i \neq j \tag{6}$$

where ρ is the density matrix and its elements are calculated from the coherent amplitudes as $\rho_{ij} = c_i c_j^*$. In the original FSSH prescription, the hops may be rejected if nuclear momenta cannot be rescaled along the direction of derivative nonadiabatic coupling, $\left\langle \psi_i \middle| \frac{\partial}{\partial R} \middle| \psi_j \right\rangle$, such that the total energy is conserved. Here, we use the neglect of back-reaction approximation (NBRA) method proposed by Craig, Duncan, and Prezhdo,[73,74] according to which nuclear momenta are not rescaled even if the hop to a new adiabatic state is accepted. Hence, the back-reaction of electronic dynamics on the nuclear one is neglected. Instead, nuclear degrees of freedom evolve adiabatically at all times. The electronic degrees of freedom evolve along such adiabatic trajectories. To ensure correct partitioning of energy between electronic and nuclear degrees of freedom, the proposed hops are accepted in the NBRA with the probability

$$P^{\mathrm{NBRA}}_{i\to j} = \min\left(1, \exp\left(-\frac{E_j - E_i}{k_{\mathrm{B}}T}\right)\right)\quad, i \neq j \tag{7}$$

in lieu of the energy conservation along the derivative NAC direction.

Since the FSSH is known to be overcoherent,[75] we also compute dynamics using two methods that introduce decoherence corrections, namely the instantaneous decoherence at attempted hops (ID-A)[76] and the modified simplified decay of mixing (mSDM),[77] which is a revision of the SDM method proposed by Granucci et al.[78] In the ID-A method, the coherent amplitude of the initial state is reset to zero, $c_i = 0$, at every attempted hop, even if the hop is not accepted. In the SDM method, the coherent amplitudes are modified at each time step using the following relations:

$$c_i^{\mathrm{new}} = c_i^{\mathrm{old}} \exp\left(-\frac{\Delta t}{\tau_{ij}}\right)\quad, i \neq j \tag{8}$$

$$c_j^{\mathrm{new}} = c_j^{\mathrm{old}} \sqrt{\frac{1 - \sum_{i\neq j} |c_i^{\mathrm{new}}|^2}{|c_j^{\mathrm{old}}|^2}} \tag{9}$$

Here, j is the active state. In the original SDM approach, the decoherence times, τ_{ij}, are usually computed according to the energy-based formula.[78] The mSDM approach also follows eqs 8 and 9 but computes these parameters using the formula proposed by Akimov and Prezhdo:[79]

$$\tau_{ij}^{-1} = \sqrt{\frac{5\delta E_{ij}^{2}}{12\hbar^2}} \tag{10}$$

where $\delta E_{ij}^{2} = \langle (E_{ij} - \bar{E}_{ij})^2 \rangle$ is the ensemble-averaged energy gap fluctuation, $E_{ij} = E_i - E_j$, and $\bar{E}_{ij} = \langle E_{ij} \rangle$.

2.2. Computational Details.

To vary the concentration of the charge carriers, we consider C_3N_4 monolayers simulation supercells of seven sizes: 2 × 2 (2.84 nm × 2.46 nm, 224 atoms), 3 × 3 (4.27 nm × 3.70 nm, 504 atoms), 4 × 4 (5.70 nm × 4.93 nm, 896 atoms), 5 × 5 (7.12 nm × 6.17 nm, 1400 atoms), 6 × 6 (8.55 nm × 7.40 nm, 2016 atoms), 8 × 8 (11.40 nm × 9.90 nm, 3584 atoms), and 10 × 10 (14.24 nm × 12.33 nm, 5600 atoms). A vacuum region of 15 Å is included above each monolayer in the simulation box. We use the CP2K[80−82] software package for MD. The electronic structure calculations are conducted using the xTB method,[42] during both the adiabatic trajectory sampling and when computing NACs along such trajectories. Within xTB methodology, a minimal valence basis of spherical Gaussian-type orbital functions is adopted for each atom that approximates a Slater-type orbital. A mixed orbital transformation (OT)[82] and diagonalization approach is used as described in more detail in our previous study.[27] The number of unoccupied orbitals used in the calculations is taken to be at least 20% of the number of occupied orbitals for better convergence. For the 10 × 10 monolayer, the total number of occupied orbitals is 12 800 and we add up to 2600 more unoccupied orbitals in the calculations. The MD calculations are performed for 3000 steps with an integration time step of 1.0 fs. The first 1000 steps are considered equilibration/thermalization steps and are disregarded in the NAC and NBRA-NA-MD calculations. The last 2000 steps of the MD trajectory are selected for NA-MD simulations. All electronic structure calculations are performed in the Γ-point with a charge density convergence limit of 10^{-6} bohr^{-3}. The band structures of the C_3N_4 unit cell and its 2 × 2 supercell are computed using DFT. We use a double-ζ-valence-polarized basis set[83] and Perdew−Burke−Ernzerhof (PBE) exchange−correlation functional[84] with a 500 Ry charge density cutoff value. The DFT-D3 dispersion correction[85] is included in the calculations. Band structure was computed along the wave vectors of M, Γ, and K.

We use Libra[86,87] for performing NA-MD simulations and computing time overlaps between MOs. Libra can efficiently compute overlaps between a large number of MOs in a Gaussian-type orbital basis using the Libint2 package.[88] For NA-MD simulations, a mixed single-particle electron and hole excitation basis is built from the ground state (GS) MO that consists of all excitations from the first 10 occupied orbitals, HOMO − 9 to HOMO, to the first 10 unoccupied orbitals, LUMO to LUMO + 9, that counts to a total number of 100 excitations. The excitations are ordered using their identities with spin-adapted configuration as is described in more detail in ref 27. The phase correction[89] and state reordering[90] are applied to the time-overlap matrices, and then NACs between pairs of excited states are computed using the Hammes-Schiffer and Tully method:[91]

$$d_{ij}\left(t + \frac{\Delta t}{2}\right) \approx \frac{\langle \psi_i(t) | \psi_j(t+\Delta t)\rangle - \langle \psi_i(t+\Delta t) | \psi_j(t)\rangle}{2\Delta t} \tag{11}$$

The NA-MD calculations are conducted using two different active spaces (bases of SD states): (a) a "two-states" model consists of only the GS and the first excited state (S_1); (b) an "*n*-states" model consists of the GS and all excited states within the range of ∼0.2 eV above S_1. The number *n* here depends on the size of the supercell used and takes the values of 24, 36, 46, 54, 56, 58, and 72 states for all the structures in order from the smallest (the 2 × 2) to the largest (the 10 × 10) ones. For each structure, 10 ps of NA-MD is computed using the "repetition" approach of Prezhdo and co-workers.[14,92,93] That is, the data sets of vibronic Hamiltonian constituting 2 ps are repeated five times, to constitute a total of 10 ps for each NA-MD trajectory. This approach has been shown to perform adequately for

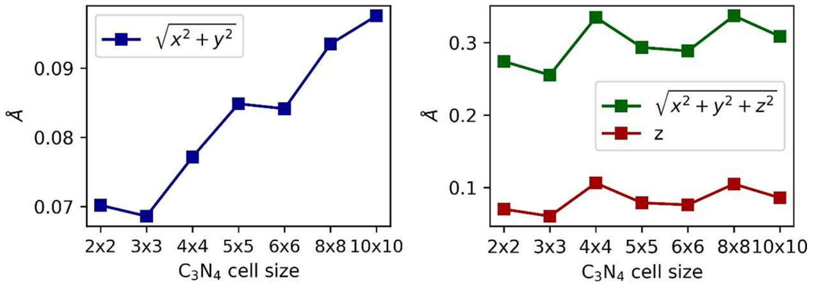

Figure 1. Characterization of atomic fluctuation in the C_3N_4 monolayers used in this work. Atomic fluctuations computed for $\sqrt{x^2+y^2}$, $\sqrt{x^2+y^2+z^2}$, and z.

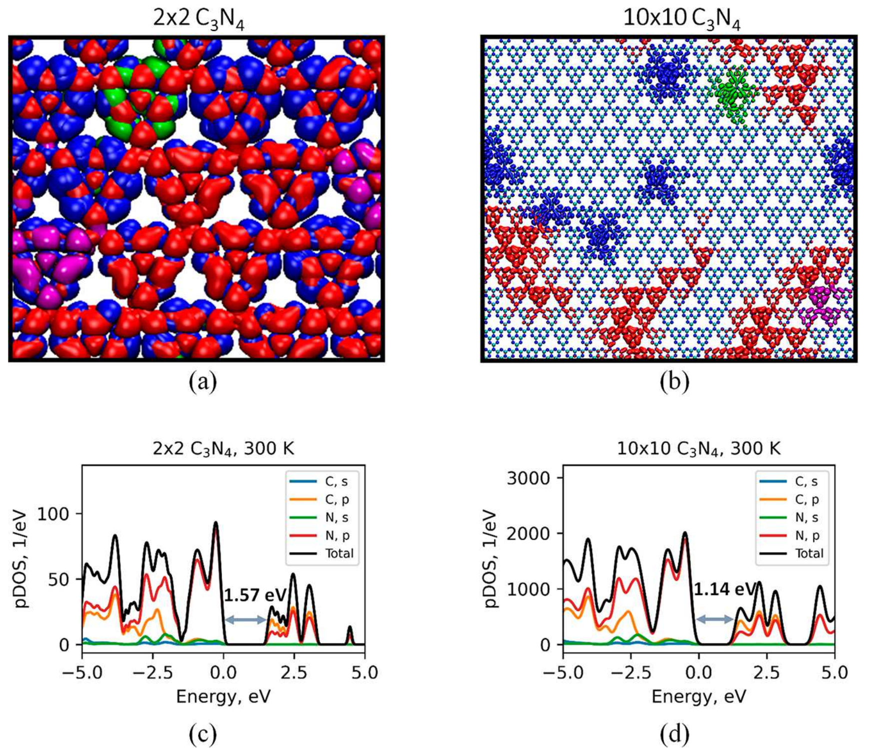

Figure 2. Isosurfaces of HOMO − 9 to HOMO and LUMO to LUMO + 9 of the (a) smallest and (b) largest C_3N_4 monolayers with an isovalue of 0.005 bohr^{-3}. The occupied and unoccupied MOs, HOMO, and LUMO are shown in blue, red, green, and purple colors, respectively. Average pDOS values over 2 ps of the equilibrated MD trajectory for the (c) smallest and (d) largest C_3N_4 monolayers. The Fermi energy level is set to zero and the average HOMO−LUMO band gaps for each structure are shown in the panels.

Hamiltonian time series of typical solid-state materials, and it can lead to variations of the time scales that are 3−5 times the true time scales.[94] For each 10 ps time series, the NA-MD starts at any of 100 points of the original 2 ps trajectory. For each calculation, 2000 stochastic surface hopping trajectories are sampled. Each such batch calculation is repeated six times for better statistics. The trajectory surface hopping calculations are conducted using the FSSH,[72] ID-A,[76] and mSDM[77,78] methods.

The time-dependent total population of the excited states, $P(t)$, is fitted with an exponential function of the form

$$P(t;\,\tau) = \exp\left(\frac{-t}{\tau}\right) \tag{12}$$

Here, τ is the corresponding e−h recombination time scale. Only the time scales with an R^2 value greater than 0.1 are selected for averaging.[27] Finally, the error bar is computed using

$$\epsilon = z_c\frac{\sigma}{\sqrt{n}} \tag{13}$$

$$\sigma = \sqrt{\frac{\sum_{i=1}^{n}(\tau_i - \overline{\tau})^2}{n-1}} \tag{14}$$

$$\overline{\tau} = \frac{1}{n}\sum_{i=1}^{n}\tau_i \tag{15}$$

Here, z_c is the Z value for the confidence level c (e.g., z_c = 1.960 for c = 95%), the confidence interval is ($\overline{\tau} - E$, $\overline{\tau} + E$), and n is the number of the acceptable fits (those with $R^2 \geq 0.1$).

In this work, we also introduce a new option in Libra input with a keyword called "together_mode", where one can

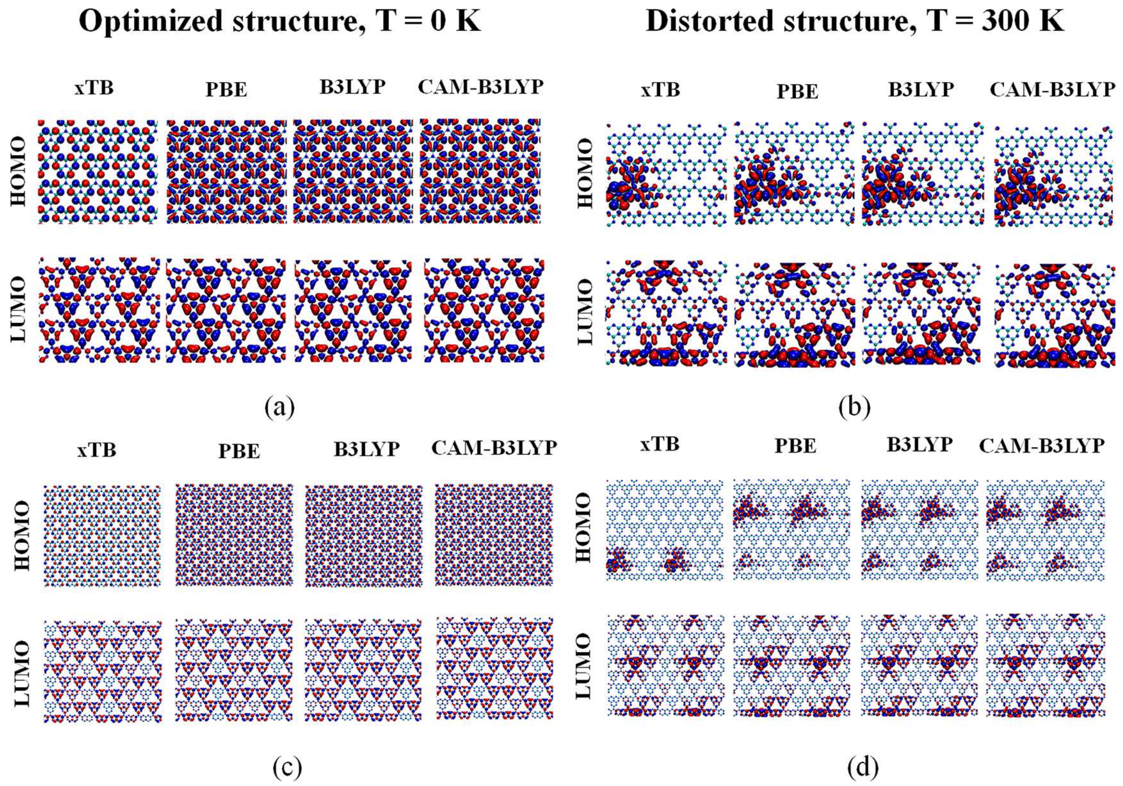

Figure 3. Comparison of orbital localization in ideal (a, c) and distorted (b, d) replicated supercells of different sizes (2 × 2 supercells, a and b; 4 × 4 supercells, c and d). Note that the larger 4 × 4 supercells are obtained by replicating the smaller 2 × 2 ones.

visualize multiple MOs for a single geometry with different colors using VMD[95] software and generate MO evolution animation.

3. RESULTS AND DISCUSSION

The analysis of molecular dynamics trajectories (which can also be observed in the orbitals' diffusion animations in the Supporting Information) indicates that all systems remain nearly flat in our simulations. Indeed, the average fluctuation of atomic coordinates in the *Z* direction (normal to the surface) is on the order of 0.08 Å, while the in-plane fluctuations are much more significant—on the order of 0.3 Å (Figure 1, Table S1). Based on these numbers, the surface corrugation of the system is nearly negligible, although Gao and co-workers[96] suggested much stronger corrugation in similar systems. The observation of the planar structure in our calculations is consistent with a number of other computational works[97−99] on this material, although several other computational works argued for a corrugated structure of C_3N_4.[100−102] Some experiments also support the distorted structure of the graphitic carbon nitride.[103−105] Furthermore, some studies suggest that the realistic graphitic carbon nitride is composed of 1D ribbons of polymer melon assembled into a 2D structure by hydrogen bonds[106,107] and hence is not well represented by the fully fused structure used in this and other works. However, the fully fused structure is suitable for the purpose of this work, where we focus on the effects of carrier concentration.

It is interesting to observe a steady increase of the in-plane fluctuations of atoms as the supercell becomes larger, even though the absolute value of such fluctuations remains small (Figure 1a). At the same time, the out-of-plane fluctuations do not show a monotonic increase with the supercell size. Such fluctuations are already larger than the in-plane ones, so the relative changes are less pronounced than for the in-plane component. Overall, the total fluctuations increase in larger supercells, suggesting the larger C_3N_4 sheets become more flexible.

The representative snapshots of the occupied and unoccupied MOs in the 2 × 2 and 10 × 10 supercells are shown in Figure 2a,b (see Figure S1 for all supercells of the C_3N_4 monolayer). Namely, Figure 2 and Figure S1 show HOMO − 9 to HOMO and LUMO to LUMO + 9, which are used to construct the basis of Slater determinants (SDs) representing mixed e−h excitations in our NA-MD simulations. The HOMO is localized roughly over a single melem (the triangular repeated motif composed of three fused rings) unit of C_3N_4, while the LUMO is somewhat more extensive, e.g., in the 10 × 10 supercell it localizes over three melem units. When focusing on the combined charge density of all the orbitals involved in the construction of the SD basis (blue and red colors in Figure 1), it appears delocalized over the entire supercell in the 2 × 2 system but having a finite size in the 10 × 10 supercell. Furthermore, the occupied orbitals are much more localized—their charge densities appear as clusters on several melem units. At the same time, the charge densities of the unoccupied orbitals appear as more continuous entities, delocalized over multiple connected melem units.

We note that such delocalization and clustering patterns are clearly visible in the extended supercells, but "disappear" in smaller cells, where one may erroneously consider them delocalized over the entire system. The orbitals exhibit constant diffusive motion (adiabatic evolution), as illustrated by the animations in the Supporting Information. The localization of MOs may be associated with the temporal symmetry breaking of the system due to thermal motion of its nuclei. In solid-state physics, this effect is known as Anderson's

https://doi.org/10.1021/acs.jpcc.3c00211
J. Phys. Chem. C 2023, 127, 9083−9096

Table 1. Average Values of Band Gap, $\hbar|\mathrm{NAC}_{i,0}|$, $\hbar|\mathrm{NAC}_{i,i+1}|$, and e−h Recombination Time Scales in the Two-States/*n*-States Model Obtained by Fitting the Dynamics to the Exponential Function in Eq 12

system	band gap, eV	$\hbar|\mathrm{NAC}_{i,0}|$, meV	$\hbar|\mathrm{NAC}_{i,i+1}|$, meV	FSSH	ID-A	mSDM
2 × 2 (2.84 nm × 2.46 nm)	1.57	0.602	108.67	65.24 ± 0.87 ps/7.12 ± 0.18 ps	65.33 ± 0.87 ps/527.70 ± 8.34 ps	506.02 ± 7.48 ps/217.16 ± 1.93 ps
3 × 3 (4.27 nm × 3.70 nm)	1.43	0.212	141.77	181.75 ± 2.04 ps/41.40 ± 1.41 ps	182.57 ± 1.96 ps/6.30 ± 0.41 ns	4.96 ± 0.31 ns/2.11 ± 0.13 ns
4 × 4 (5.70 nm × 4.93 nm)	1.37	0.101	130.15	1.04 ± 0.02 ns/146.56 ± 5.08 ps	1.06 ± 0.02 ns/15.27 ± 0.96 ns	15.28 ± 0.97 ns/8.39 ± 0.57 ns
5 × 5 (7.12 nm × 6.17 nm)	1.29	0.047	123.64	7.09 ± 0.51 ns/531.10 ± 19.15 ps	6.97 ± 0.47 ns/20.07 ± 1.50 ns	20.74 ± 1.82 ns/17.36 ± 1.11 ns
6 × 6 (8.55 nm × 7.40 nm)	1.25	0.024	117.95	10.42 ± 0.64 ns/1.74 ± 0.13 ns	11.14 ± 0.70 ns/22.08 ± 2.23 ns	22.76 ± 2.30 ns/20.07 ± 1.54 ns
8 × 8 (11.40 nm × 9.90 nm)	1.15	0.006	105.95	23.44 ± 2.73 ns/15.39 ± 0.94 ns	21.34 ± 2.04 ns/23.02 ± 6.89 ns	17.98 ± 3.36 ns/19.87 ± 3.58 ns
10 × 10 (14.24 nm × 12.33 nm)	1.14	0.003	97.63	18.73 ± 6.21 ns/18.73 ± 6.21 ns	23.02 ± 6.91 ns/23.02 ± 6.91 ns	18.28 ± 3.90 ns/18.28 ± 3.90 ns

localization;[108,109] in chemistry it is discussed within the exciton self-trapping mechanism.[110−113] However, the localization can also be ascribed to Coulombic and exchange interactions of electrons.

To investigate the origin of orbital localization, we have set up the following additional calculations: a smaller system (2 × 2 supercell) is periodically replicated several times into a larger 4 × 4 supercell and the orbitals for the two kinds of systems are compared with each other (Figure 3, Figures S2 and S3). Since the two types of supercells are related by periodic translation, one could anticipate that the band structures obtained in the two kinds of calculations should be similar to each other, if not identical. Indeed, we observe that the band gaps in two types of calculations are nearly the same, regardless of the original replicated geometry, whether it is the optimized or distorted one sampled by MD (Table S2). Also, one may expect that orbitals computed in smaller supercells would periodically replicate in larger supercells congruently with the periodic replication of the atomic structure. We observe such a replication, especially in highly symmetric structures (Figure 3a,c). However, in distorted systems such a replication is incomplete and dies off with the distance from the "central" image (Figure 3b,d). This partial repetition breaking could be due to increased degeneracies of orbitals in larger systems. For instance, we observe a 9-fold degeneracy of HOMO and HOMO − 1 levels in the 10 × 10 supercells (Table S3). Thus, the MOs shown in Figure 3 constitute only a subset of such state manifolds. In addition, the incomplete replication of orbitals could be a consequence of using the minimalistic *k*-point grids in our calculations (only a single *k*-point for the evaluation of the electronic density in the SCF iterations). This matter will be investigated in greater detail in a separate work. The degree of the repetition breaking is different for various type of Hamiltonians and is greatest for the xTB Hamiltonian as compared to PBE or hybrid functional calculations. Such a dependence may be attributed to the effective range of exchange interactions, which differs for each Hamiltonian and leads to different degeneracies and spatial extents of the orbitals. We observe only a weak dependence of the orbital sizes on the choice of electronic structure methodology (Figure 3). The xTB orbitals are the most localized ones compared to the generalized gradient approximation (GGA) and hybrid density functional calculations, although the xTB orbitals are still in reasonable agreement with the DFT orbitals. On the basis of the above results, we conclude that the orbital localization is induced primarily by the molecular structure disorder, hence following the Anderson/exciton self-trapping mechanism.

As a consequence of different orbital localizations in smaller and larger supercells, we also observe a difference in the computed time overlaps and hence NACs (Table S4). More localized orbitals in larger supercells lead to smaller time overlaps and hence smaller NACs. We note though that the decrease of the NAC values in larger supercells may also be a consequence of using orbitals that constitute single objects taken from the manifolds of degenerate sets of orbitals. Using superpositions of such degenerate orbitals, as for example could be the case in TD-DFT(B) calculations, would likely enhance the overlaps and could lead to larger NACs and faster dynamics, in line with our earlier results.[11,28]

Band structure calculations are conducted for the C_3N_4 monolayer unit cell and the 2 × 2 supercell (see Figure S4). Our calculations indicate that the band structure of the unit cell folds well into that one of the 2 × 2 supercell. The frontier bands are nearly flat, so the system can be regarded as a direct gap semiconductor and the electronic dynamics can be described using a single *k*-point (Γ-point in this work). The plots of the average partial density of states (pDOS) over all equilibrated geometries show that, as one moves to larger structures, the DOS increases but the overall character of the MOs does not change (Figure 2c,d). The occupied orbitals are mostly localized on N p atoms, and the unoccupied orbitals have both C p and N p character. If the pDOSs are mapped to the three components of the p orbitals, i.e., p_x, p_y, and p_z, one observes that the band edge occupied orbitals have mostly N p_z component with a similar contribution of the p_x and p_y orbitals, which is due to the symmetry of the structure, and the unoccupied orbitals have mostly C p_z character and N p_z character, respectively (see Figure S5). The average values of the band gap at 300 K varies from 1.14 to 1.57 eV with respect to system size and decreases with increasing supercell size (Table 1). The computed band gap values using xTB are smaller than the ones computed previously using DFT calculations. Agrawal et al.[37] showed that, for a C_3N_4 monolayer unit cell, the PBE[84] and HSE06[114] functionals show band gaps of 1.92 (PBE) and 3.26 eV (HSE06), respectively. The experimentally reported band gap is at the 2.79 eV value.[115] Thus, we conclude that the xTB values are underestimated compared to both the more accurate theory and the experiment. Because the energy gap and NAC values

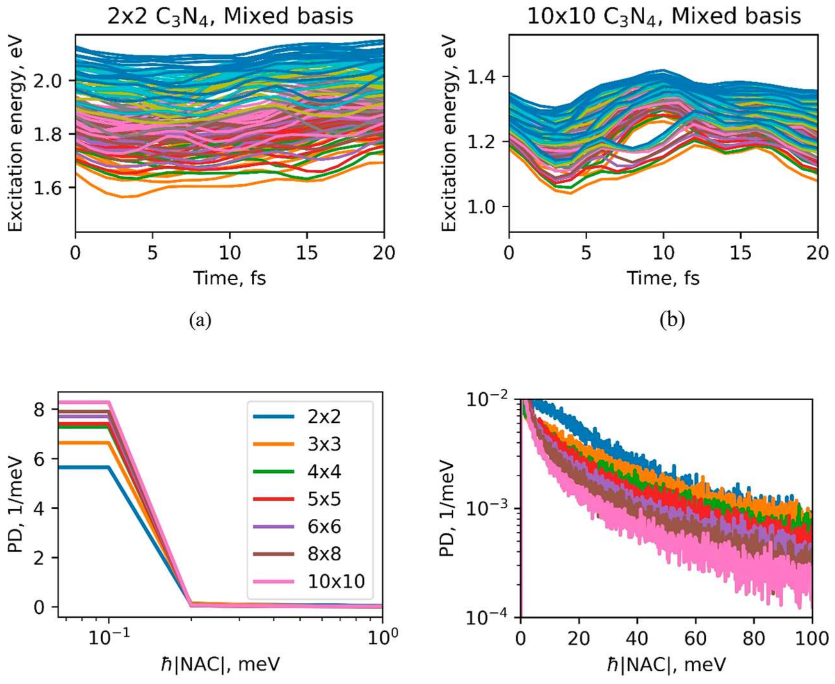

(a) (b) (c) (d)

Figure 4. Probability distribution of NAC magnitudes computed for all pairs of identity-ordered mixed electron and hole excitations with excitation energies of ∼0.2 eV above S_1. Snapshots of the evolution of the energy levels in the identity-ordered mixed electron and hole basis for the (a) smallest and (b) largest structures for 20 fs. The distribution is shown for two ħ|NAC| value ranges of (c) 0−1 meV and (d) 0−100 meV.

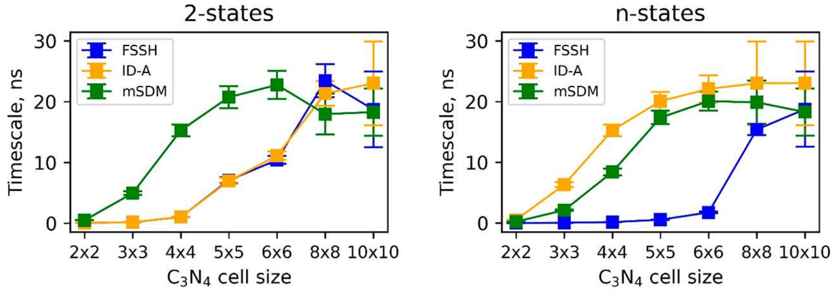

(a) (b)

Figure 5. Electron−hole recombination dynamics time scales for different structures in the (a) two-states and (b) *n*-states models. The *n* values for each structure from the smallest to largest ones are 26, 36, 46, 54, 56, 58, and 72, respectively.

are roughly inversely proportional,[116] we may expect that the NACs between the ground and excited states used in this work are overestimated over more realistic values and that the obtained time scales could constitute the lower bounds to the realistic time scales. At the same time, we anticipate that the trends observed in this work shall remain relatively invariant with the change of electronic structure methodology, although more detailed investigations would be required to fully support this assumption.

As our analysis of the orbital localization suggests, orbitals are more distant from each other on average in larger supercells (Figure 2a,b). As a result, we expect smaller average time overlaps in larger supercells. The time variation of the time overlaps is related to the NAC between excited states. Hence, the time variations of smaller time overlaps would result in smaller average NACs. Indeed, we observe that the average values of ħ|NAC| between the GS and excited states decrease as one moves to larger structures (see Table 1).

The NACs can also be analyzed using the probability distribution of the NAC magnitudes between all pairs of excited states in the mixed electron and hole excitation basis. The ħ|NAC| values are generated over 2000 geometries of the MD simulation for each monolayer. We observe that, despite the higher density of states in the larger structures (Figure 4a,b and Figures S5 and S6), the frequency of larger NAC values is higher in smaller simulation supercells, while the probability to sample smaller values of ħ|NAC| (e.g., $<10^{-1}$ meV) is higher in larger simulation supercells (Figure 4c,d). This observation is consistent with the trend previously observed in silicon nanoclusters of varied size.[27] The NAC values may be correlated to the degree of orbital degeneracy. As we discussed above, orbitals appear more localized in larger systems due to the intrinsically higher degeneracy of orbitals combined with the breaking of this degeneracy by nuclear disorder, causing the known Anderson localization.[108,109] One may think of the following mnemonic mechanism: a single band of a smaller supercell must be "supported" by a set of several degenerate orbitals (here, we use the term "orbitals" since the bands become flatter in larger systems) of the larger supercell. Picking only one of such orbitals out of the manifold of degenerate

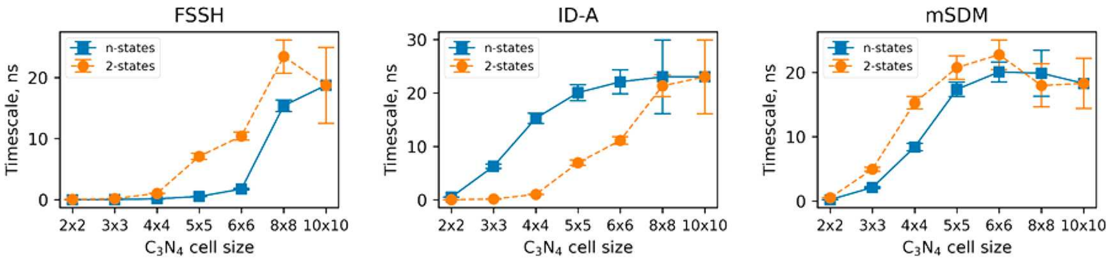

(a) (b) (c)

Figure 6. Results of the electron−hole recombination dynamics for all supercells of the C_3N_4 monolayers in two- and *n*-states models using (a) FSSH, (b) ID-A, and (c) mSDM methods. The *n* values for each structure from the smallest to largest ones are 26, 36, 46, 54, 56, 58, and 72, respectively.

states when computing NACs inevitably leads to only a partial representation of the smaller-cell band, leading to decreased time overlaps and hence decreased NAC values. On the basis of this analysis of the NAC distributions, we anticipate slower recombination dynamics and hence longer recombination time scales in larger systems. However, one question still remains unanswered: Does such a dependence remain in effect for all carrier concentrations, or is there a critical threshold after which the supercell size will not matter?

To address the above question, we explicitly compute the e−h recombination time scales with their corresponding error bars using FSSH, ID-A, and mSDM (Figure 5). The time scales are obtained by fitting the GS recovery population with the function in eq 12. The detailed fits for all the methods and systems are summarized in Figures S7−S12. Our calculations indicate that the recombination time scales increase as the simulation supercell size increases; however, they all reach an upper bound limit that corresponds to the concentration-independent recombination times. The curves saturate more clearly (and earlier) when decoherence effects are accounted for. For instance, the mSDM method predicts a convergence to the concentration-independent time scales already in the 5 × 5 supercell (Figure 5a,b), whereas FSSH (no decoherence) and ID-A show signs of a saturation starting only from supercells as large as 8 × 8 (in the two-states model, Figure 5a). Including more states in the active space of simulations facilitates earlier convergence of computed recombination time scales in smaller supercells. For instance, the ID-A decoherence method predicts the convergence in a 8 × 8 supercell if only two states are included in the active space (Figure 5a) and in a 5 × 5 supercell if more states are included in it (Figure 5b). In the latter case, it behaves similarly to the mSDM method. Including many states in the active space does not make the FSSH time scales converge faster (so it still requires an about 8 × 8 supercell to reach the concentration-independent values) but makes the transition more abrupt and clear (compare Figure 5, panels a and b, blue lines).

The observed convergence of the time scales at the system size of an about 6 × 6 supercell may be also related to the system size at which the orbitals included in the active space start occupying only a fraction of the supercell area, instead of being delocalized over the entire supercell (Figure S1). At this point, the quantum "confinement" (this term is used only loosely since this is a periodic system) effects become vanishing, and the orbital time overlaps are determined by the intrinsic average size of the orbitals included in the active space and not by the extent the orbitals are artificially "compressed" due to the finite size of the simulation cell. The further extension of the simulation supercell affects the time overlaps of these orbitals only slightly.

It is instructive to compare the e−h recombination dynamics as a function of the number of active states used in NA dynamics. In our calculations, the S_1 state is initially populated. In the minimalistic model with only two states, the only possible transition is to the ground electronic state (GS). The NAC magnitude is of determining importance in this scenario, while the density of states is not an important factor. In the *n*-states calculations, more excited states are included in the active space than before, and the population can transiently transfer to higher energy states due to NACs between those states and small energy gaps between them. In this case, the population can directly transfer to the GS from those transiently populated states. Previously, we showed that increasing the number of states in the active space can accelerate the NA dynamics.[27] In the present work, we also observe an acceleration of the dynamics in the *n*-states model compared to the two-states one, although only when using the FSSH and mSDM methods (Figure 6a,c). Indeed, both the FSSH and mSDM algorithms support a mechanism of population and coherence transfer from S_1 to all of the higher-energy states, followed by a "parallel" population transfer from all of these states to the GS. We refer the reader to our earlier work for a more detailed discussion of this mechanism and another numerical demonstration.[27] Interestingly, the ID-A methodology (e.g., Figure 6b) leads to a deceleration of the recombination dynamics when the active space is extended. This effect can be rationalized as follows: in the systems with the higher densities of states (i.e., in the *n*-states model as opposed to the two-states one), the attempted hops are more probable. Since the coherent dynamics in the ID-A is "reset" after each attempted hop, the "resets" are more frequent in the systems with the larger number of active states, where the attempted hops are more frequent, hence leading to the overall population transfer deceleration.

Finally, it is interesting to note that the density of states does not play a notable role in determining the time scales in the largest systems, e.g., 8 × 8 supercells and up, regardless of the method used (FSSH, ID-A, or mSDM). Indeed, the time scales computed using both the two-states and *n*-states models are comparable in those cases. Our rationalization of this result is as follows: as one increases the supercell size, the NACs between any of the excited states and the GS become so negligible compared to the couplings between the S_1 and the higher-energy states that the internal dynamics within the manifold of excited states is "seen" as instantaneous from the perspective of the GS. In this regard, the entire manifold of the

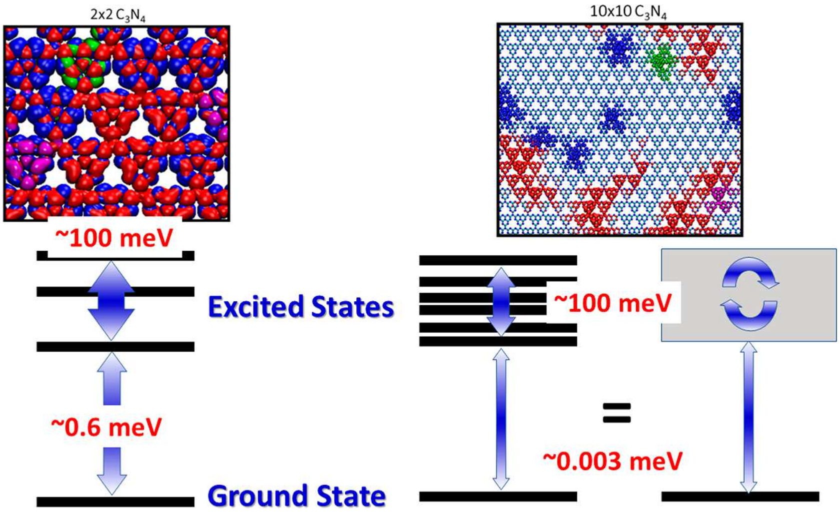

Figure 7. Schematic representation of the *n*-states model "reduction" to an effective two-states model. (left) In small supercells, the ratio of the NACs between excited state pairs to the NACs between excited states and the GS is moderate, so all individual excited states do play a notable role. (right) In large supercells, the NACs between excited states and the GS are notably smaller than the NACs between the pairs of excited states, so the entire manifold of the excited states behaves as a single effective state.

excited states is seen as a single state, effectively reducing the "*n*-states" model to the two-states one. As was discussed earlier, the decoherence methods do not notably change the dynamics in two-level systems.[36] The proposed mechanism of effective reduction of the "*n*-states" model into the two-states one in the largest systems (e.g., 8 × 8 supercells and up) also causes all the tested methods (FSSH, ID-A, and mSDM) to yield comparable time scales. The "reduction" mechanism is supported by our calculations of the average NAC magnitudes between the pairs of excited states included in the active space, $\hbar|\mathrm{NAC}_{i,i+1}|$, and the average NAC magnitudes between each excited state and the GS, $\hbar|\mathrm{NAC}_{i,0}|$ (Table 1). Going from the 2 × 2 supercell to the 10 × 10 supercell, we observe only a minor variation of $\hbar|\mathrm{NAC}_{i,i+1}|$, which remains on the order of 100 meV in all systems. However, the ground-to-excited-state coupling, $\hbar|\mathrm{NAC}_{i,0}|$, varies by several orders of magnitude, from an average of ca. 0.6 meV in the 2 × 2 system to about 0.003 meV in the 10 × 10 system (Figure 7). Although 0.6 meV coupling is already significantly smaller than 100 meV, one may still expect some effect of the intra-excited-states-manifold dynamics on the e−h recombination dynamics. Increasing this discrepancy of the NAC magnitudes by several orders of magnitude contributes to further separation of the time scales for the intraband and e−h recombination dynamics, thus making the collective manifold of excited states behave as a single effective state.

Although the proposed "reduction" mechanism is a plausible explanation, we also leave the possibility that the results for the largest systems could be affected by the numerical issues. For the largest 10 × 10 monolayer used in this study, the NAC values between the GS and excited states are very small and may be affected by the numerical issues. Furthermore, for the systems with very small NACs, the population decay may not be observed in short simulation trajectories, especially when decoherence schemes are used (Figures S7−S12). Hence, using the "repetition" approach in these cases is essential. As mentioned in Computational Details, such a repetition approach may lead to a 3−5 times variation of the predicted time scale from the true value, but larger differences are possible for intrinsically slow processes.

We briefly discuss our current results in view of existing experimental and computational studies. The experimentally derived recombination time scales are on the order of 7.3 and 6.4 ns for monolayer and bulk C_3N_4, respectively.[35] Earlier, the computational studies of Agrawal et al.[37] reported the recombination time scales of 10.8 and 3.4 ns for monolayer and bulk C_3N_4 using the PBE functional and the decoherence induced surface hopping (DISH) method.[73,74,117] Our present calculations on the monolayer structures converge to about 18−23 ns values in the largest structures used. Our rates are only a factor of 2−3 smaller than the supposed rates from the experiment or the rates reported by Agrawal et al.[37] However, these differences should be taken critically. First of all, the fully fused, 2D graphitic carbon nitride structure used in this work (as well as by others) is questioned by some researchers. For instance, Lau and co-workers suggested that the experimentally relevant C_3N_4 structure was in fact a heptazine-based 1D polymer melon, composed of ribbons assembled into a 2D structure by hydrogen bonds.[106,107] Thus, the direct assessment of the computationally derived time scales (both in this work and in the one by Agrawal et al.[37]) is complicated. Comparing to the results of Agrawal et al.,[37] our calculations yield slower dynamics, which could be attributed to the electronic structure methodology and to the concentration effects. This difference can be attributed to both the difference in charge carrier concentration and the difference in electronic structure calculations (PBE versus xTB). Furthermore, the xTB methodology used in this work led to the underestimated band gap. Hence, one could expect that our recombination rates would be overestimated.[116] On the other hand, accounting for the many-body effects of excited states as opposed to the single-particle description adopted in this work could lead to additional acceleration of the recombination dynamics,[28] compensating for the functional-choice effect and potentially bringing the computed time scales closer to the experimental ones. As a result, our time scales are comparable to the experimentally reported values, within the assumption that one could do such a comparison, keeping in mind the potential difference of the molecular structures of C_3N_4 in computations and in experiment.

In passing, we comment on some limitations, approximations, and goals of this work not yet discussed above. First of all, we do not aim to reach the experimentally accessible carrier concentrations but rather focus on revealing possible qualitative and semiquantitative trends. Such time scale renormalization could in principle be performed using the method recently developed by Wang et al.[39] We also neglect other effects that may be relevant at high carrier concentrations, such as Auger[118−120] or singlet fission processes,[121−124] exciton and polyexciton formation, and dissociation. Accounting for such effects would require using much more computationally expensive approaches, inapplicable to systems of the considered sizes. Even going beyond the single-particle approximation[11,28,125] used in the present work may be a notable challenge with the systems of the size scale considered. Such studies may still be feasible though and can be the next round of refinement of the current results.

4. CONCLUSIONS

In this work, we address the question of the role of charge carrier concentration in e−h recombination dynamics. We demonstrate how the NA-MD/xTB approach developed earlier[27] can be applied to study the NA-MD in unprecedentedly sized systems with up to 5600 atoms. We focus on the e−h recombination dynamics in graphitic carbon nitride (C_3N_4) monolayer. With the above approach, we have been able to conduct NA-MD calculations in supercells extending their sizes from 2.8 nm × 2.5 nm (224 atoms) to 14.2 nm × 12.3 nm (5600 atoms) and explore the extent to which the e−h recombination time scales depend on the carrier concentration.

Our calculations indicate a strong dependence of the e−h recombination times on the size of simulation supercell and hence on the formal charge carrier concentration. The time scales vary from 65 ps in the smallest (2 × 2) system to 23 ns in the largest (8 × 8, 10 × 10) ones, when a minimalistic two-states model is used. The range of variation of the recombination time scales reduces to 7 ps in the 2 × 2 supercell and to 18 ns in 8 × 8 and 10 × 10 supercells when the basis of electronic excitations is increased. For small and intermediate size supercells, the time scales are generally sensitive to the inclusion of decoherence effects: both mSDM and ID-A methods which introduce such effects predict a notably slower recombination than the FSSH method that does not account for electronic decoherence. The only exception is the minimalistic two-states model, for which the ID-A and FSSH results virtually coincide.

Last, but not least, despite the strong dependence of the recombination time scales on the charge carrier concentration, the NA-MD methodology, and the active space of electronic excitation, we observe a convergence of the predicted time scales with the size of simulation supercell, not just a monotonic unbound increase of such values with the system size. The inclusion of decoherence effects facilitates such a convergence, making the time scales independent of system size already in smaller systems, e.g., in 5 × 5 supercells. Furthermore, the converged values depend neither on the size of the excitation basis nor on the inclusion of decoherence effects. We explain this invariance of the converged values by an effective "reduction" of the *n*-states model to an effective two-states model caused by the discrepancy in the NAC magnitudes between the pairs of excited states and the excited−ground state pairs that is growing as the supercell's size increases. The converged time scales vary in the 18−23 ns range and are achieved in the 8 × 8 or larger systems with the few exceptions when they are achieved in the smaller systems, as mentioned above. The found time scales are comparable to the experimentally reported time scales, although the direct comparison is complicated due to potential differences in molecular structures, as discussed. Our time scales are also comparable to the computational values of Agrawal et al.,[37] although achieved in much larger simulation supercells.

■ ASSOCIATED CONTENT

Data Availability Statement

Detailed scripts and input files used for all types of calculations are available in digital form online at the Zenodo repository[126] at https://doi.org/10.5281/Zenodo.7507728.

SI Supporting Information

The Supporting Information is available free of charge at https://pubs.acs.org/doi/10.1021/acs.jpcc.3c00211.

Molecular orbital isosurfaces; pDOS, evolution of excited state energy levels; e−h recombination dynamics results (PDF)

Evolution of occupied and unoccupied molecular orbitals for 2 × 2 supercell (MP4)

Evolution of occupied and unoccupied molecular orbitals for 3 × 3 supercell (MP4)

Evolution of occupied and unoccupied molecular orbitals for 4 × 4 supercell (MP4)

Evolution of occupied and unoccupied molecular orbitals for 5 × 5 supercell (MP4)

Evolution of occupied and unoccupied molecular orbitals for 6 × 6 supercell (MP4)

Evolution of occupied and unoccupied molecular orbitals for 8 × 8 supercell (MP4)

Evolution of occupied and unoccupied molecular orbitals for 10 × 10 supercell (MP4)

■ AUTHOR INFORMATION

Corresponding Author

Alexey V. Akimov − *Department of Chemistry, University at Buffalo, State University of New York, Buffalo, New York 14260, United States;* orcid.org/0000-0002-7815-3731; Email: alexeyak@buffalo.edu

Author

Mohammad Shakiba − *Department of Chemistry, University at Buffalo, State University of New York, Buffalo, New York 14260, United States*

Complete contact information is available at: https://pubs.acs.org/10.1021/acs.jpcc.3c00211

Notes

The authors declare no competing financial interest.

■ ACKNOWLEDGMENTS

A.V.A. acknowledges the financial support of the National Science Foundation (Grant OAC-NSF-1931366). Support of computations is provided by the Center for Computational Research at the University at Buffalo.

■ REFERENCES

(1) Sarkar, R.; Kar, M.; Habib, M.; Zhou, G.; Frauenheim, T.; Sarkar, P.; Pal, S.; Prezhdo, O. V. Common Defects Accelerate Charge Separation and Reduce Recombination in CNT/Molecule Compo-

sites: Atomistic Quantum Dynamics. *J. Am. Chem. Soc.* **2021**, *143* (17), 6649−6656.

(2) Li, W.; Zhou, L.; Prezhdo, O. V.; Akimov, A. V. Spin-Orbit Interactions Greatly Accelerate Nonradiative Dynamics in Lead Halide Perovskites. *ACS Energy Letters* **2018**, *3* (9), 2159−2166.

(3) Kilina, S.; Velizhanin, K. A.; Ivanov, S.; Prezhdo, O. V.; Tretiak, S. Surface Ligands Increase Photoexcitation Relaxation Rates in CdSe Quantum Dots. *ACS Nano* **2012**, *6* (7), 6515−6524.

(4) Yazdani, N.; Bozyigit, D.; Vuttivorakulchai, K.; Luisier, M.; Infante, I.; Wood, V. Tuning Electron-Phonon Interactions in Nanocrystals through Surface Termination. *Nano Lett.* **2018**, *18* (4), 2233−2242.

(5) Boehme, S. C.; ten Brinck, S.; Maes, J.; Yazdani, N.; Zapata, F.; Chen, K.; Wood, V.; Hodgkiss, J. M.; Hens, Z.; Geiregat, P.; Infante, I. Phonon-Mediated and Weakly Size-Dependent Electron and Hole Cooling in CsPbBr3 Nanocrystals Revealed by Atomistic Simulations and Ultrafast Spectroscopy. *Nano Lett.* **2020**, *20* (3), 1819−1829.

(6) She, Y.; Hou, Z.; Prezhdo, O. V.; Li, W. Identifying and Passivating Killer Defects in Pb-Free Double Cs2AgBiBr6 Perovskite. *J. Phys. Chem. Lett.* **2021**, *12* (43), 10581−10588.

(7) Jiang, X.; Zheng, Q.; Lan, Z.; Saidi, W. A.; Ren, X.; Zhao, J. Real-Time GW-BSE Investigations on Spin-Valley Exciton Dynamics in Monolayer Transition Metal Dichalcogenide. *Science Advances* **2021**, *7* (10), No. eabf3759.

(8) Chu, W.; Saidi, W. A.; Zhao, J.; Prezhdo, O. V. Soft Lattice and Defect Covalency Rationalize Tolerance of *β*-CsPbI3 Perovskite Solar Cells to Native Defects. *Angew. Chem., Int. Ed.* **2020**, *59* (16), 6435−6441.

(9) Lystrom, L.; Tamukong, P.; Mihaylov, D.; Kilina, S. Phonon-Driven Energy Relaxation in PbS/CdS and PbSe/CdSe Core/Shell Quantum Dots. *J. Phys. Chem. Lett.* **2020**, *11* (11), 4269−4278.

(10) Han, Y.; Kilin, D. S. Nonradiative Relaxation Dynamics of a Cesium Lead Halide Perovskite Photovoltaic Architecture: Effect of External Electric Fields. *J. Phys. Chem. Lett.* **2020**, *11* (23), 9983−9989.

(11) Smith, B.; Shakiba, M.; Akimov, A. V. Crystal Symmetry and Static Electron Correlation Greatly Accelerate Nonradiative Dynamics in Lead Halide Perovskites. *J. Phys. Chem. Lett.* **2021**, *12* (9), 2444−2453.

(12) Yu, Z.; Pan, Y.; Shen, Y.; Wang, Z.; Ong, Z.-Y.; Xu, T.; Xin, R.; Pan, L.; Wang, B.; Sun, L.; Wang, J.; Zhang, G.; Zhang, Y. W.; Shi, Y.; Wang, X. Towards Intrinsic Charge Transport in Monolayer Molybdenum Disulfide by Defect and Interface Engineering. *Nat. Commun.* **2014**, *5* (1), 5290.

(13) He, J.; Long, R. Lead Vacancy Can. Explain the Suppressed Nonradiative Electron-Hole Recombination in FAPbI3 Perovskite under Iodine-Rich Conditions: A Time-Domain Ab Initio Study. *journal of physical chemistry letters* **2018**, *9* (22), 6489−6495.

(14) Long, R.; Fang, W.; Prezhdo, O. V. Moderate Humidity Delays Electron-Hole Recombination in Hybrid Organic-Inorganic Perovskites: Time-Domain Ab Initio Simulations Rationalize Experiments. *J. Phys. Chem. Lett.* **2016**, *7* (16), 3215−3222.

(15) Yang, Y.; Fang, W.-H.; Benderskii, A.; Long, R.; Prezhdo, O. V. Strain Controls Charge Carrier Lifetimes in Monolayer WSe2: Ab Initio Time Domain Analysis. *J. Phys. Chem. Lett.* **2019**, *10* (24), 7732−7739.

(16) Climent, C.; Barbatti, M.; Wolf, M. O.; Bardeen, C. J.; Casanova, D. The Photophysics of Naphthalene Dimers Controlled by Sulfur Bridge Oxidation. *Chemical Science* **2017**, *8* (7), 4941−4950.

(17) Hoff, D. A.; da Silva, R.; Rego, L. G. C. Coupled Electron-Hole Quantum Dynamics on D-*π*-A Dye-Sensitized TiO2 Semiconductors. *J. Phys. Chem. C* **2012**, *116* (40), 21169−21178.

(18) Oliboni, R. S.; Yan, H.; Fan, H.; Abraham, B.; Avenoso, J. P.; Galoppini, E.; Batista, V. S.; Gundlach, L.; Rego, L. G. C. Vibronic Effects in the Ultrafast Interfacial Electron Transfer of Perylene-Sensitized TiO2 Surfaces. *J. Phys. Chem. C* **2019**, *123* (20), 12599−12607.

(19) Ha, Y.; Park, J.-G.; Hong, K.-H.; Kim, H. Enhanced Light Emission through Symmetry Engineering of Halide Perovskites. *J. Am. Chem. Soc.* **2022**, *144* (1), 297−305.

(20) Akimov, A. V.; Neukirch, A. J.; Prezhdo, O. V. Theoretical Insights into Photoinduced Charge Transfer and Catalysis at Oxide Interfaces. *Chem. Rev.* **2013**, *113* (6), 4496−4565.

(21) Akimov, A. V.; Asahi, R.; Jinnouchi, R.; Prezhdo, O. V. What Makes the Photocatalytic CO $_2$ Reduction on N-Doped Ta $_2$ O $_5$ Efficient: Insights from Nonadiabatic Molecular Dynamics. *J. Am. Chem. Soc.* **2015**, *137* (35), 11517−11525.

(22) Niu, X.; Bai, X.; Zhou, Z.; Wang, J. Rational Design and Characterization of Direct Z-Scheme Photocatalyst for Overall Water Splitting from Excited State Dynamics Simulations. *ACS Catal.* **2020**, *10* (3), 1976−1983.

(23) Senanayake, R. D.; Aikens, C. M. Theoretical Investigation of Relaxation Dynamics in the Au18 (SH) 14 Thiolate-Protected Gold Nanocluster. *J. Chem. Phys.* **2019**, *151* (9), 094702.

(24) Senanayake, R. D.; Guidez, E. B.; Neukirch, A. J.; Prezhdo, O. V.; Aikens, C. M. Theoretical Investigation of Relaxation Dynamics in Au $_{38}$ (SH) $_{24}$ Thiolate-Protected Gold Nanoclusters. *J. Phys. Chem. C* **2018**, *122* (28), 16380−16388.

(25) Senanayake, R. D.; Akimov, A. V.; Aikens, C. M. Theoretical Investigation of Electron and Nuclear Dynamics in the $[$Au $_{25}$ (SH) $_{18}]$ $^{-1}$ Thiolate-Protected Gold Nanocluster. *J. Phys. Chem. C* **2017**, *121* (20), 10653−10662.

(26) Toldo, J. M.; do Casal, M. T.; Barbatti, M. Mechanistic Aspects of the Photophysics of UVA Filters Based on Meldrum Derivatives. *J. Phys. Chem. A* **2021**, *125* (25), 5499−5508.

(27) Shakiba, M.; Stippell, E.; Li, W.; Akimov, A. V. Nonadiabatic Molecular Dynamics with Extended Density Functional Tight-Binding: Application to Nanocrystals and Periodic Solids. *J. Chem. Theory Comput.* **2022**, *18* (9), 5157−5180.

(28) Smith, B.; Shakiba, M.; Akimov, A. V. Nonadiabatic Dynamics in Si and CdSe Nanoclusters: Many-Body vs Single-Particle Treatment of Excited States. *J. Chem. Theory Comput.* **2021**, *17* (2), 678−693.

(29) Zhang, L.; Vasenko, A. S.; Zhao, J.; Prezhdo, O. V. Mono-Elemental Properties of 2D Black Phosphorus Ensure Extended Charge Carrier Lifetimes under Oxidation: Time-Domain Ab Initio Analysis. *J. Phys. Chem. Lett.* **2019**, *10* (5), 1083−1091.

(30) Guo, H.; Chu, W.; Zheng, Q.; Zhao, J. Tuning the Carrier Lifetime in Black Phosphorene through Family Atom Doping. *J. Phys. Chem. Lett.* **2020**, *11* (12), 4662−4667.

(31) Giannini, S.; Blumberger, J. Charge Transport in Organic Semiconductors: The Perspective from Nonadiabatic Molecular Dynamics. *Acc. Chem. Res.* **2022**, *55* (6), 819−830.

(32) Giannini, S.; Carof, A.; Blumberger, J. Crossover from Hopping to Band-Like Charge Transport in an Organic Semiconductor Model: Atomistic Nonadiabatic Molecular Dynamics Simulation. *J. Phys. Chem. Lett.* **2018**, *9* (11), 3116−3123.

(33) Shen, M.; Zhang, L.; Wang, M.; Tian, J.; Jin, X.; Guo, L.; Wang, L.; Shi, J. Carbon-Vacancy Modified Graphitic Carbon Nitride: Enhanced CO 2 Photocatalytic Reduction Performance and Mechanism Probing. *Journal of Materials Chemistry A* **2019**, *7* (4), 1556−1563.

(34) Jin, X.; Fan, X.; Tian, J.; Cheng, R.; Li, M.; Zhang, L. MoS 2 Quantum Dot Decorated G-C 3 N 4 Composite Photocatalyst with Enhanced Hydrogen Evolution Performance. *RSC Adv.* **2016**, *6* (58), 52611−52619.

(35) Lin, Q.; Li, L.; Liang, S.; Liu, M.; Bi, J.; Wu, L. Efficient Synthesis of Monolayer Carbon Nitride 2D Nanosheet with Tunable Concentration and Enhanced Visible-Light Photocatalytic Activities. *Applied Catalysis B: Environmental* **2015**, *163*, 135−142.

(36) Akimov, A. V. Excited State Dynamics in Monolayer Black Phosphorus Revisited: Accounting for Many-Body Effects. *J. Chem. Phys.* **2021**, *155* (13), 134106.

(37) Agrawal, S.; Lin, W.; Prezhdo, O. V.; Trivedi, D. J. Ab Initio Quantum Dynamics of Charge Carriers in Graphitic Carbon Nitride Nanosheets. *J. Chem. Phys.* **2020**, *153* (5), 054701.

(38) Nie, Z.; Shi, Y.; Qin, S.; Wang, Y.; Jiang, H.; Zheng, Q.; Cui, Y.; Meng, Y.; Song, F.; Wang, X.; Turcu, I. C. E.; Wang, X.; Xu, Y.; Shi, Y.; Zhao, J.; Zhang, R.; Wang, F. Tailoring Exciton Dynamics of Monolayer Transition Metal Dichalcogenides by Interfacial Electron-Phonon Coupling. *Commun. Phys.* **2019**, *2* (1), 1−8.

(39) Wang, S.; Huang, M.; Wu, Y.-N.; Chu, W.; Zhao, J.; Walsh, A.; Gong, X.-G.; Wei, S.-H.; Chen, S. Effective Lifetime of Non-Equilibrium Carriers in Semiconductors from Non-Adiabatic Molecular Dynamics Simulations. *Nat. Comput. Sci.* **2022**, *2* (8), 486−493.

(40) Hu, W.; Yang, J. Two-Dimensional van Der Waals Heterojunctions for Functional Materials and Devices. *Journal of Materials Chemistry C* **2017**, *5* (47), 12289−12297.

(41) Rudenko, A. N.; Brener, S.; Katsnelson, M. I. Intrinsic Charge Carrier Mobility in Single-Layer Black Phosphorus. *Phys. Rev. Lett.* **2016**, *116* (24), 246401.

(42) Bannwarth, C.; Ehlert, S.; Grimme, S. GFN2-XTB—An Accurate and Broadly Parametrized Self-Consistent Tight-Binding Quantum Chemical Method with Multipole Electrostatics and Density-Dependent Dispersion Contributions. *J. Chem. Theory Comput.* **2019**, *15* (3), 1652−1671.

(43) Grimme, S.; Bannwarth, C.; Shushkov, P. A Robust and Accurate Tight-Binding Quantum Chemical Method for Structures, Vibrational Frequencies, and Noncovalent Interactions of Large Molecular Systems Parametrized for All Spd-Block Elements (Z = 1−86). *J. Chem. Theory Comput.* **2017**, *13* (5), 1989−2009.

(44) Bannwarth, C.; Caldeweyher, E.; Ehlert, S.; Hansen, A.; Pracht, P.; Seibert, J.; Spicher, S.; Grimme, S. Extended Tight-Binding Quantum Chemistry Methods. *WIREs: Computational Molecular Science* **2021**, *11* (2), No. e1493.

(45) Porezag, D.; Frauenheim, Th.; Köhler, Th.; Seifert, G.; Kaschner, R. Construction of Tight-Binding-like Potentials on the Basis of Density-Functional Theory: Application to Carbon. *Phys. Rev. B* **1995**, *51* (19), 12947−12957.

(46) Seifert, G.; Porezag, D.; Frauenheim, Th. Calculations of Molecules, Clusters, and Solids with a Simplified LCAO-DFT-LDA Scheme. *Int. J. Quantum Chem.* **1996**, *58* (2), 185−192.

(47) Elstner, M.; Porezag, D.; Jungnickel, G.; Elsner, J.; Haugk, M.; Frauenheim, Th.; Suhai, S.; Seifert, G. Self-Consistent-Charge Density-Functional Tight-Binding Method for Simulations of Complex Materials Properties. *Phys. Rev. B* **1998**, *58* (11), 7260−7268.

(48) Smith, B.; Akimov, A. V. Hot Electron Cooling in Silicon Nanoclusters via Landau-Zener Nonadiabatic Molecular Dynamics: Size Dependence and Role of Surface Termination. *J. Phys. Chem. Lett.* **2020**, *11* (4), 1456−1465.

(49) Lee, I. S.; Ha, J.-K.; Han, D.; Kim, T. I.; Moon, S. W.; Min, S. K. PyUNIxMD: A Python-Based Excited State Molecular Dynamics Package. *J. Comput. Chem.* **2021**, *42* (24), 1755−1766.

(50) Uratani, H.; Nakai, H. Scalable Ehrenfest Molecular Dynamics Exploiting the Locality of Density-Functional Tight-Binding Hamiltonian. *J. Chem. Theory Comput.* **2021**, *17* (12), 7384−7396.

(51) Uratani, H.; Nakai, H. Non-Adiabatic Molecular Dynamics with Divide-and-Conquer Type Large-Scale Excited-State Calculations. *J. Chem. Phys.* **2020**, *152* (22), 224109.

(52) Dewar, M. J.; Zoebisch, E. G.; Healy, E. F.; Stewart, J. J. Development and Use of Quantum Mechanical Molecular Models. 76. AM1: A New General Purpose Quantum Mechanical Molecular Model. *J. Am. Chem. Soc.* **1985**, *107* (13), 3902−3909.

(53) Stewart, J. J. Optimization of Parameters for Semiempirical Methods I. Method. *Journal of computational chemistry* **1989**, *10* (2), 209−220.

(54) Malone, W.; Nebgen, B.; White, A.; Zhang, Y.; Song, H.; Bjorgaard, J. A.; Sifain, A. E.; Rodriguez-Hernandez, B.; Freixas, V. M.; Fernandez-Alberti, S.; et al. NEXMD Software Package for Nonadiabatic Excited State Molecular Dynamics Simulations. *J. Chem. Theory Comput.* **2020**, *16* (9), 5771−5783.

(55) Nelson, T. R.; White, A. J.; Bjorgaard, J. A.; Sifain, A. E.; Zhang, Y.; Nebgen, B.; Fernandez-Alberti, S.; Mozyrsky, D.; Roitberg, A. E.; Tretiak, S. Non-Adiabatic Excited-State Molecular Dynamics: Theory and Applications for Modeling Photophysics in Extended Molecular Materials. *Chem. Rev.* **2020**, *120* (4), 2215−2287.

(56) Seibert, J.; Bannwarth, C.; Grimme, S. Biomolecular Structure Information from High-Speed Quantum Mechanical Electronic Spectra Calculation. *J. Am. Chem. Soc.* **2017**, *139* (34), 11682−11685.

(57) Caldeweyher, E.; Ehlert, S.; Hansen, A.; Neugebauer, H.; Spicher, S.; Bannwarth, C.; Grimme, S. A Generally Applicable Atomic-Charge Dependent London Dispersion Correction. *J. Chem. Phys.* **2019**, *150* (15), 154122.

(58) Bursch, M.; Neugebauer, H.; Grimme, S. Structure Optimisation of Large Transition-Metal Complexes with Extended Tight-Binding Methods. *Angew. Chem., Int. Ed.* **2019**, *58* (32), 11078−11087.

(59) Praus, P. A Brief Review of S-Triazine Graphitic Carbon Nitride. *Carbon Lett.* **2022**, *32*, 703.

(60) Wang, X.; Maeda, K.; Thomas, A.; Takanabe, K.; Xin, G.; Carlsson, J. M.; Domen, K.; Antonietti, M. A Metal-Free Polymeric Photocatalyst for Hydrogen Production from Water under Visible Light. *Nat. Mater.* **2009**, *8* (1), 76−80.

(61) Zhao, G.; Yang, H.; Liu, M.; Xu, X. Metal-Free Graphitic Carbon Nitride Photocatalyst Goes Into Two-Dimensional Time. *Frontiers in Chemistry* **2018**, *6*, 551.

(62) Agrawal, S.; Vasenko, A. S.; Trivedi, D. J.; Prezhdo, O. V. Charge Carrier Nonadiabatic Dynamics in Non-Metal Doped Graphitic Carbon Nitride. *J. Chem. Phys.* **2022**, *156* (9), 094702.

(63) Gumber, S.; Agrawal, S.; Prezhdo, O. V. Excited State Dynamics in Dual-Defects Modified Graphitic Carbon Nitride. *J. Phys. Chem. Lett.* **2022**, *13* (4), 1033−1041.

(64) Pei, X.; Fang, Q.; Long, R. Tuning the Nonradiative Electron-Hole Recombination with Defects in Monolayer Black Phosphorus. *J. Phys. Chem. Lett.* **2022**, *13* (43), 10162−10168.

(65) Wei, Y.; Long, R. Grain Boundaries Are Benign and Suppress Nonradiative Electron-Hole Recombination in Monolayer Black Phosphorus: A Time-Domain Ab Initio Study. *J. Phys. Chem. Lett.* **2018**, *9* (14), 3856−3862.

(66) Long, R.; Fang, W.; Akimov, A. V. Nonradiative Electron-Hole Recombination Rate Is Greatly Reduced by Defects in Monolayer Black Phosphorus: Ab Initio Time Domain Study. *J. Phys. Chem. Lett.* **2016**, *7* (4), 653−659.

(67) Esteban-Puyuelo, R.; Sanyal, B. Role of Defects in Ultrafast Charge Recombination in Monolayer MoS 2. *Phys. Rev. B* **2021**, *103* (23), 235433.

(68) Akimov, A. V. Fundamentals of Trajectory-Based Methods for Nonadiabatic Dynamics. In *Reference Module in Chemistry, Molecular Sciences and Chemical Engineering*; Elsevier: 2022. DOI: 10.1016/B978-0-12-821978-2.00034-9.

(69) Smith, B.; Akimov, A. V. Modeling Nonadiabatic Dynamics in Condensed Matter Materials: Some Recent Advances and Applications. *J. Phys.: Condens. Matter* **2020**, *32* (7), 073001.

(70) Crespo-Otero, R.; Barbatti, M. Recent Advances and Perspectives on Nonadiabatic Mixed Quantum-Classical Dynamics. *Chem. Rev.* **2018**, *118* (15), 7026−7068.

(71) Nikitin, E. *Theory of Elementary Atomic and Molecular Processes in Gases*; Clarendon Press: 1974.

(72) Tully, J. C. Molecular Dynamics with Electronic Transitions. *J. Chem. Phys.* **1990**, *93* (2), 1061−1071.

(73) Craig, C. F.; Duncan, W. R.; Prezhdo, O. V. Trajectory Surface Hopping in the Time-Dependent Kohn-Sham Approach for Electron-Nuclear Dynamics. *Physical review letters* **2005**, *95* (16), 163001.

(74) Duncan, W. R.; Craig, C. F.; Prezhdo, O. V. Time-Domain Ab Initio Study of Charge Relaxation and Recombination in Dye-Sensitized TiO2. *J. Am. Chem. Soc.* **2007**, *129* (27), 8528−8543.

(75) Landry, B. R.; Subotnik, J. E. Communication: Standard Surface Hopping Predicts Incorrect Scaling for Marcus' Golden-Rule Rate: The Decoherence Problem Cannot Be Ignored. *J. Chem. Phys.* **2011**, *135* (19), 191101.

(76) Nelson, T.; Fernandez-Alberti, S.; Roitberg, A. E.; Tretiak, S. Nonadiabatic Excited-State Molecular Dynamics: Treatment of Electronic Decoherence. *J. Chem. Phys.* **2013**, *138* (22), 224111.

(77) Smith, B.; Akimov, A. V. A Comparative Analysis of Surface Hopping Acceptance and Decoherence Algorithms within the Neglect of Back-Reaction Approximation. *J. Chem. Phys.* **2019**, *151* (12), 124107.

(78) Granucci, G.; Persico, M. Critical Appraisal of the Fewest Switches Algorithm for Surface Hopping. *J. Chem. Phys.* **2007**, *126* (13), 134114.

(79) Akimov, A. V.; Prezhdo, O. V. Persistent Electronic Coherence Despite Rapid Loss of Electron-Nuclear Correlation. *J. Phys. Chem. Lett.* **2013**, *4* (22), 3857−3864.

(80) Kühne, T. D.; Iannuzzi, M.; Del Ben, M.; Rybkin, V. V.; Seewald, P.; Stein, F.; Laino, T.; Khaliullin, R. Z.; Schütt, O.; Schiffmann, F.; Golze, D.; Wilhelm, J.; Chulkov, S.; Bani-Hashemian, M. H.; Weber, V.; Borštnik, U.; Taillefumier, M.; Jakobovits, A. S.; Lazzaro, A.; Pabst, H.; Müller, T.; Schade, R.; Guidon, M.; Andermatt, S.; Holmberg, N.; Schenter, G. K.; Hehn, A.; Bussy, A.; Belleflamme, F.; Tabacchi, G.; Glöß, A.; Lass, M.; Bethune, I.; Mundy, C. J.; Plessl, C.; Watkins, M.; VandeVondele, J.; Krack, M.; Hutter, J. CP2K: An Electronic Structure and Molecular Dynamics Software Package - Quickstep: Efficient and Accurate Electronic Structure Calculations. *J. Chem. Phys.* **2020**, *152* (19), 194103.

(81) Hutter, J.; Iannuzzi, M.; Schiffmann, F.; VandeVondele, J. Cp2k: Atomistic Simulations of Condensed Matter Systems. *Wiley Interdisciplinary Reviews: Computational Molecular Science* **2014**, *4* (1), 15−25.

(82) VandeVondele, J.; Krack, M.; Mohamed, F.; Parrinello, M.; Chassaing, T.; Hutter, J. Quickstep: Fast and Accurate Density Functional Calculations Using a Mixed Gaussian and Plane Waves Approach. *Comput. Phys. Commun.* **2005**, *167* (2), 103−128.

(83) VandeVondele, J.; Hutter, J. Gaussian Basis Sets for Accurate Calculations on Molecular Systems in Gas and Condensed Phases. *J. Chem. Phys.* **2007**, *127* (11), 114105.

(84) Perdew, J. P.; Burke, K.; Ernzerhof, M. Generalized Gradient Approximation Made Simple. *Phys. Rev. Lett.* **1996**, *77* (18), 3865−3868.

(85) Grimme, S.; Antony, J.; Ehrlich, S.; Krieg, H. A Consistent and Accurate *Ab Initio* Parametrization of Density Functional Dispersion Correction (DFT-D) for the 94 Elements H-Pu. *J. Chem. Phys.* **2010**, *132* (15), 154104.

(86) Shakiba, M.; Smith, B.; Li, W.; Dutra, M.; Jain, A.; Sun, X.; Garashchuk, S.; Akimov, A. Libra: A Modular Software Library for Quantum Nonadiabatic Dynamics. *Software Impacts* **2022**, *14*, 100445.

(87) Akimov, A. V. Libra: An Open-Source "Methodology Discovery" Library for Quantum and Classical Dynamics Simulations: SOFTWARE NEWS AND UPDATES. *J. Comput. Chem.* **2016**, *37* (17), 1626−1649.

(88) Valeev, E. F. *Libint: A Library for the Evaluation of Molecular Integrals of Many-Body Operators over Gaussian Functions*, ver. 2.8.0. http://libint.valeyev.net/.

(89) Akimov, A. V. A Simple Phase Correction Makes a Big Difference in Nonadiabatic Molecular Dynamics. *journal of physical chemistry letters* **2018**, *9* (20), 6096−6102.

(90) Fernandez-Alberti, S.; Roitberg, A. E.; Nelson, T.; Tretiak, S. Identification of Unavoided Crossings in Nonadiabatic Photoexcited Dynamics Involving Multiple Electronic States in Polyatomic Conjugated Molecules. *J. Chem. Phys.* **2012**, *137* (1), 014512.

(91) Hammes-Schiffer, S.; Tully, J. C. Proton Transfer in Solution: Molecular Dynamics with Quantum Transitions. *J. Chem. Phys.* **1994**, *101* (6), 4657−4667.

(92) Li, L.; Long, R.; Bertolini, T.; Prezhdo, O. V. Sulfur Adatom and Vacancy Accelerate Charge Recombination in MoS2 but by Different Mechanisms: Time-Domain Ab Initio Analysis. *Nano Lett.* **2017**, *17* (12), 7962−7967.

(93) Li, L.; Long, R.; Prezhdo, O. V. Why Chemical Vapor Deposition Grown MoS2 Samples Outperform Physical Vapor Deposition Samples: Time-Domain Ab Initio Analysis. *Nano Lett.* **2018**, *18* (6), 4008−4014.

(94) Li, W.; Akimov, A. V. How Good Is the Vibronic Hamiltonian Repetition Approach for Long-Time Nonadiabatic Molecular Dynamics? *J. Phys. Chem. Lett.* **2022**, *13* (41), 9688−9694.

(95) Humphrey, W.; Dalke, A.; Schulten, K. VMD: Visual Molecular Dynamics. *J. Mol. Graphics* **1996**, *14* (1), 33−38.

(96) Gao, Q.; Zhuang, X.; Hu, S.; Hu, Z. Corrugation Matters: Structure Models of Single Layer Heptazine-Based Graphitic Carbon Nitride from First-Principles Studies. *J. Phys. Chem. C* **2020**, *124* (8), 4644−4651.

(97) Ma, X.; Lv, Y.; Xu, J.; Liu, Y.; Zhang, R.; Zhu, Y. A Strategy of Enhancing the Photoactivity of G-C3N4 via Doping of Nonmetal Elements: A First-Principles Study. *J. Phys. Chem. C* **2012**, *116* (44), 23485−23493.

(98) Zuluaga, S.; Liu, L.-H.; Shafiq, N.; Rupich, S. M.; Veyan, J.-F.; Chabal, Y. J.; Thonhauser, T. Structural Band-Gap Tuning in g-C3N4. *Phys. Chem. Chem. Phys.* **2015**, *17* (2), 957−962.

(99) Choudhuri, I.; Bhattacharyya, G.; Kumar, S.; Pathak, B. Metal-Free Half-Metallicity in a High Energy Phase C-Doped Gh-C3N4 System: A High Curie Temperature Planar System. *J. Mater. Chem. C* **2016**, *4* (48), 11530−11539.

(100) Ji, Y.; Dong, H.; Lin, H.; Zhang, L.; Hou, T.; Li, Y. Heptazine-Based Graphitic Carbon Nitride as an Effective Hydrogen Purification Membrane. *RSC Adv.* **2016**, *6* (57), 52377−52383.

(101) Azofra, L. M.; MacFarlane, D. R.; Sun, C. A DFT Study of Planar vs. Corrugated Graphene-like Carbon Nitride (g-C3N4) and Its Role in the Catalytic Performance of CO2 Conversion. *Phys. Chem. Chem. Phys.* **2016**, *18* (27), 18507−18514.

(102) Wu, H.-Z.; Liu, L.-M.; Zhao, S.-J. The Effect of Water on the Structural, Electronic and Photocatalytic Properties of Graphitic Carbon Nitride. *Phys. Chem. Chem. Phys.* **2014**, *16* (7), 3299−3304.

(103) Chen, Y.; Wang, B.; Lin, S.; Zhang, Y.; Wang, X. Activation of n → Π* Transitions in Two-Dimensional Conjugated Polymers for Visible Light Photocatalysis. *J. Phys. Chem. C* **2014**, *118* (51), 29981−29989.

(104) Zhao, H.; Yu, H.; Quan, X.; Chen, S.; Zhao, H.; Wang, H. Atomic Single Layer Graphitic-C3N4: Fabrication and Its High Photocatalytic Performance under Visible Light Irradiation. *RSC Adv.* **2014**, *4* (2), 624−628.

(105) Xu, J.; Zhang, L.; Shi, R.; Zhu, Y. Chemical Exfoliation of Graphitic Carbon Nitride for Efficient Heterogeneous Photocatalysis. *J. Mater. Chem. A* **2013**, *1* (46), 14766−14772.

(106) Lau, V. W.; Moudrakovski, I.; Botari, T.; Weinberger, S.; Mesch, M. B.; Duppel, V.; Senker, J.; Blum, V.; Lotsch, B. V. Rational Design of Carbon Nitride Photocatalysts by Identification of Cyanamide Defects as Catalytically Relevant Sites. *Nat. Commun.* **2016**, *7* (1), 12165.

(107) Lau, V. W.; Yu, V. W.; Ehrat, F.; Botari, T.; Moudrakovski, I.; Simon, T.; Duppel, V.; Medina, E.; Stolarczyk, J. K.; Feldmann, J.; Blum, V.; Lotsch, B. V. Urea-Modified Carbon Nitrides: Enhancing Photocatalytic Hydrogen Evolution by Rational Defect Engineering. *Adv. Energy Mater.* **2017**, *7* (12), 1602251.

(108) Anderson, P. W. Absence of Diffusion in Certain Random Lattices. *Phys. Rev.* **1958**, *109* (5), 1492−1505.

(109) Abrahams, E.; Anderson, P. W.; Licciardello, D. C.; Ramakrishnan, T. V. Scaling Theory of Localization: Absence of Quantum Diffusion in Two Dimensions. *Phys. Rev. Lett.* **1979**, *42* (10), 673−676.

(110) Soler, M. A.; Roitberg, A. E.; Nelson, T.; Tretiak, S.; Fernandez-Alberti, S. Analysis of State-Specific Vibrations Coupled to the Unidirectional Energy Transfer in Conjugated Dendrimers. *J. Phys. Chem. A* **2012**, *116* (40), 9802−9810.

(111) Fernandez-Alberti, S.; Makhov, D. V.; Tretiak, S.; Shalashilin, D. V. Non-Adiabatic Excited State Molecular Dynamics of Phenylene Ethynylene Dendrimer Using a Multiconfigurational Ehrenfest Approach. *Phys. Chem. Chem. Phys.* **2016**, *18* (15), 10028−10040.

(112) Ondarse-Alvarez, D.; Kömürlü, S.; Roitberg, A. E.; Pierdominici-Sottile, G.; Tretiak, S.; Fernandez-Alberti, S. D.;

Kleiman, V. Ultrafast Electronic Energy Relaxation in a Conjugated Dendrimer Leading to Inter-Branch Energy Redistribution. *Phys. Chem. Chem. Phys.* **2016**, *18* (36), 25080−25089.

(113) Freixas, V. M.; Ondarse-Alvarez, D.; Tretiak, S.; Makhov, D. V.; Shalashilin, D. V.; Fernandez-Alberti, S. Photoinduced Non-Adiabatic Energy Transfer Pathways in Dendrimer Building Blocks. *J. Chem. Phys.* **2019**, *150* (12), 124301.

(114) Krukau, A. V.; Vydrov, O. A.; Izmaylov, A. F.; Scuseria, G. E. Influence of the Exchange Screening Parameter on the Performance of Screened Hybrid Functionals. *J. Chem. Phys.* **2006**, *125* (22), 224106.

(115) Shi, A.; Li, H.; Yin, S.; Liu, B.; Zhang, J.; Wang, Y. Effect of Conjugation Degree and Delocalized π-System on the Photocatalytic Activity of Single Layer g-C3N4. *Applied Catalysis B: Environmental* **2017**, *218*, 137−146.

(116) Lin, Y.; Akimov, A. V. Dependence of Nonadiabatic Couplings with Kohn-Sham Orbitals on the Choice of Density Functional: Pure vs Hybrid. *J. Phys. Chem. A* **2016**, *120* (45), 9028−9041.

(117) Jaeger, H. M.; Fischer, S.; Prezhdo, O. V. Decoherence-Induced Surface Hopping. *J. Chem. Phys.* **2012**, *137* (22), 22A545.

(118) Trivedi, D. J.; Wang, L.; Prezhdo, O. V. Auger-Mediated Electron Relaxation Is Robust to Deep Hole Traps: Time-Domain Ab Initio Study of CdSe Quantum Dots. *Nano Lett.* **2015**, *15* (3), 2086−2091.

(119) Zhou, G.; Lu, G.; Prezhdo, O. V. Modeling Auger Processes with Nonadiabatic Molecular Dynamics. *Nano Lett.* **2021**, *21* (1), 756−761.

(120) Dong, S.; Pal, S.; Lian, J.; Chan, Y.; Prezhdo, O. V.; Loh, Z.-H. Sub-Picosecond Auger-Mediated Hole-Trapping Dynamics in Colloidal CdSe/CdS Core/Shell Nanoplatelets. *ACS Nano* **2016**, *10* (10), 9370−9378.

(121) Akimov, A. V.; Prezhdo, O. V. Nonadiabatic Dynamics of Charge Transfer and Singlet Fission at the Pentacene/C60 Interface. *J. Am. Chem. Soc.* **2014**, *136* (4), 1599−1608.

(122) Tao, G. Understanding Electronically Non-Adiabatic Relaxation Dynamics in Singlet Fission. *J. Chem. Theory Comput.* **2015**, *11* (1), 28−36.

(123) Busby, E.; Berkelbach, T. C.; Kumar, B.; Chernikov, A.; Zhong, Y.; Hlaing, H.; Zhu, X.-Y.; Heinz, T. F.; Hybertsen, M. S.; Sfeir, M. Y.; Reichman, D. R.; Nuckolls, C.; Yaffe, O. Multiphonon Relaxation Slows Singlet Fission in Crystalline Hexacene. *J. Am. Chem. Soc.* **2014**, *136* (30), 10654−10660.

(124) Chan, W.-L.; Berkelbach, T. C.; Provorse, M. R.; Monahan, N. R.; Tritsch, J. R.; Hybertsen, M. S.; Reichman, D. R.; Gao, J.; Zhu, X.-Y. The Quantum Coherent Mechanism for Singlet Fission: Experiment and Theory. *Acc. Chem. Res.* **2013**, *46* (6), 1321−1329.

(125) Uratani, H.; Nakai, H. Simulating the Coupled Structural-Electronic Dynamics of Photo-Excited Lead Iodide Perovskites. *J. Phys. Chem. Lett.* **2020**, *11*, 4448−4455.

(126) Shakiba, M. AkimovLab/Project-C3N4: Project_C3N4_carrier_concentration, ver. 1.0.0. *Zenodo*, January 5, 2023. https://doi.org/10.5281/Zenodo.7507728.